



HAL
open science

Large-eddy simulation of thin film evaporation and condensation from a hot plate in enclosure: First order statistics

Carlo Cintolesi, Andrea Petronio, Vincenzo Armenio

► **To cite this version:**

Carlo Cintolesi, Andrea Petronio, Vincenzo Armenio. Large-eddy simulation of thin film evaporation and condensation from a hot plate in enclosure: First order statistics. *International Journal of Heat and Mass Transfer*, 2016, 101, pp.1123-1137. 10.1016/j.ijheatmasstransfer.2016.06.006 . hal-02070281

HAL Id: hal-02070281

<https://hal.science/hal-02070281>

Submitted on 17 Mar 2019

HAL is a multi-disciplinary open access archive for the deposit and dissemination of scientific research documents, whether they are published or not. The documents may come from teaching and research institutions in France or abroad, or from public or private research centers.

L'archive ouverte pluridisciplinaire **HAL**, est destinée au dépôt et à la diffusion de documents scientifiques de niveau recherche, publiés ou non, émanant des établissements d'enseignement et de recherche français ou étrangers, des laboratoires publics ou privés.

Large-eddy simulation of thin film evaporation and condensation from a hot plate in enclosure: First order statistics

Carlo Cintolesi^{a,*}, Andrea Petronio^b, Vincenzo Armenio^a

^aUniversity of Trieste, Dipartimento di Ingegneria e Architettura, Piazzale Europa 1, I-34127 Trieste, Italy

^bIEFLUIDS S.r.l., Piazzale Europa 1, I-34127 Trieste, Italy

Abstract

Numerical investigation of water evaporation and condensation in buoyancy driven flow, along with the thermal coupling between fluid and surrounding solids, is interesting for many industrial applications. The physical complexity of the evaporation and condensation processes, the mutual thermal influence of water change of phase and solid-fluid heat transfer, the anisotropy of turbulence quantities are challenging problems from numerical and theoretical side. The archetypal case of a vertical hot plate inside a cold square enclosure, filled with humid air, is studied. The solid surfaces are wetted by a thin water film. The plate cooling process due to film evaporation is analysed. Numerical simulation adopts the large-eddy methodology along with the dynamic Lagrangian sub-grid scale model. The conjugate heat transfer technique accounts for the solid-fluid thermal coupling, while the water phase is modelled under the thin film assumption. First, a preliminary case with isothermal solid boundaries and fixed film thickness is reproduced at $Ra = 5 \times 10^8$. The absence of surface heat transfer leads to analogous distribution of temperature and humidity. The cavity is characterised by strong stratification that confines the motion in the upper part. The same setting is used to simulate the case of dry air. It is found that the presence of vapour increases the velocity by a maximum of 20%. Also, the heat transfer generated by the water change of phase, in case of humid air, overcomes the other heat transfer modes. Successively, conjugate heat transfer and water film model are activated, and three cases are studied changing the plate material. The specific heat ρC_p of materials is the parameter controlling the plate cooling process, that is mainly due to evaporation and the evolution of the thermodynamic field within the enclosure. An analysis of the dew-point temperature suggests that recondensation onto the plate surface cannot occur, even for materials that are rapidly cooled.

Keywords: LES, natural convection; conjugate heat transfer; thin film; evaporation; condensation

NOTE: this is the final version of the manuscript accepted for publication. Reference to the published article:

Carlo Cintolesi, Andrea Petronio, Vincenzo Armenio. *Large-eddy simulation of thin film evaporation and condensation from a hot plate in enclosure: First order statistics*. Int. Journal of Heat and Mass Transfer 101 (2016) 1123–1137. doi:[dx.doi.org/10.1016/j.jheatmasstransfer.2016.06.006](https://doi.org/10.1016/j.jheatmasstransfer.2016.06.006)

© 2017. This manuscript version is made available under the Creative Commons [CC-BY-NC-ND 4.0](https://creativecommons.org/licenses/by-nc-nd/4.0/) license.

1. Introduction

Natural convection in presence of water evaporation and condensation plays a crucial role in a number of natural and industrial processes. A realistic and accurate numerical reproduction of such phenomena is a challenging problem from both numerical and theoretical viewpoints.

Several physical effects can influence the natural convective systems: thermal radiation from solid bodies as

well as from fluid medium; thermal-fluid interaction between solid and fluid media; Dufour and Soret effects; the fog formation in case of high humidity. From a numerical point of view, in most applications, flows cannot be considered laminar and an accurate reproduction of turbulence is required. Moreover, the Boussinesq approximation for incompressible flow, cannot be applied in systems with high temperature and humidity differences.

A detailed description of evaporation and condensation on wetted surfaces, can be found in de Gennes [10] and Oron *et al.* [24]. Thiele [34] gave also an overview on the complex physical processes involved. Heat transfer mechanisms occurring in such flows are addressed in Incropera *et al.* [15], Welty *et al.* [35], and Lienhard [22].

*Corresponding author.

Email addresses: carlo.cintolesi@gmail.com
(Carlo Cintolesi), a.petronio@iefluids.com (Andrea Petronio),
armenio@dica.units.it (Vincenzo Armenio)

In many works oriented toward practical applications, the complex interaction between liquid phase and solid surfaces is modelled through the thin film assumption: water is considered distributed over the solid surface as a continuous thin film, even if it can spread like liquid patches or sessile droplets.

Russo *et al.* [28] used Direct Numerical Simulations (DNS) to simulate a low Reynolds number turbulent channel flow. A Lagrangian model was used to simulate the water droplet distribution in air. The effects of heat and mass transfer by evaporation/condensation on the wall-normal distribution of the temperature statistics of the droplets were investigated.

The same approach was used by Bukhvostova *et al.* [6], where compressible and incompressible solvers were tested and compared. The same turbulent droplets-laden channel flow as in ref. [28] was studied. The compressible and incompressible approaches showed similar results for fluid dynamics quantities, but relevant discrepancies for thermal quantities were evidenced. The authors concluded that, overall, the compressible solver is more accurate.

Many other works investigated the effects of evaporation and condensation in closed systems, in the laminar-flow regime.

The paper of Sun *et al.* [32] reports an accurate study of laminar natural convection in different geometries, using a compressible low-Mach number model. The case of a two-dimensional square cavity was mostly analysed. A thin film of liquid water wets the walls and the domain is filled with humid air. Condensation and evaporation phenomena occur when the temperature of external walls is increased or decreased in time. The general features of the fluid motion were discussed, together with the time evolution of the averaged temperature and density, and the spatial distribution of the liquid film. The presence of circular motion near the vertical walls and Rayleigh-Bénard cells near the horizontal ones, strongly influence the distribution of water film. On the contrary, the film thickness was shown to be nearly independent on variations of the wall temperature.

Laaroussi and Lauriat [17] studied a two-dimensional square cavity. The compressible low-Mach approach was adopted, and the thermal coupling between fluid and the solid boundaries of finite thickness was simulated. The cavity has two differentially heated vertical walls, one with constant temperature and the other cooled by means of the heat exchange with the surrounding environment. Different initial configurations were taken into account. It turned out that the solid boundaries interact with fluid mixture leading to non negligible effects: in transient regime the thickness of the bounding walls influence the condensation rate, while the solid temperature distribution changes with respect to the relative humidity of the fluid. From a numerical point of view, it was pointed out that low-Mach number solution depends on the initial conditions. A comparison between compressible low-Mach and incompressible Boussinesq approach was also performed.

The two methods gave similar results when the initial temperature was uniform and equal to the average of the wall temperatures.

Similar investigation was carried out by Costa [8]: first the case of Sun *et al.* [32] was replicated, then the case of two-dimensional duct of circular cross section was analysed. Although, overall, the thermo-fluid dynamic field was similar to that of the square cavity case, some features were different (for example the Rayleigh-Bénard cells were not detected).

The forced channel flow is also a widely studied case, both numerically and experimentally. The work of Huang *et al.* [14] focused on the heat and mass transfer in a rectangular duct, with water film evaporation and condensation over the horizontal walls and an uniform inflow of moist air. Simulations were carried out for three-dimensional, steady-state flow in laminar regime. The Boussinesq approximation was adopted. A wide range of simulations were performed, changing the temperature of wetted walls, the relative humidity, the Reynolds number of the inlet flow and also the aspect ratio of the duct. Talukdar *et al.* [33] investigated the vapour mass flux released from a horizontal water pool. Simulations of a three-dimensional rectangular duct, were validated in a laminar regime.

Experiments on the same case were performed by Iskra and Simonson [16], both for laminar and turbulent regimes. The effects of forced convection on evaporation were investigated by varying the velocity of the air passing through the duct.

Raimundo *et al.* [27] proposed an analysis of the phenomena of evaporation and condensation at heated water free surface. Both simulations and experiments were carried out. The numerical solver used the Reynolds-Averaged Navier-Stokes (RANS) approach, with a two-layers $k - \epsilon$ turbulence model. The flow was assumed incompressible and a local computation of thermal-physical parameters was employed instead of the usual Boussinesq approximation. The experimental facilities consisted of a test chamber in wind tunnel. The dependence of the evaporation/condensation rate on air-water temperature difference, relative humidity and airflow velocity were analysed. It turned out that the airflow is the most influencing factor.

The natural convection in cavity filled with one or several obstacles is also of great importance in many real applications. Laguerre *et al.* [19] performed an interesting analysis of the domestic refrigerators. Numerical studies of natural convection with heat and moisture transfer in a rectangular cavity containing a homogeneous distribution of sphere [18] and cylinders [20] were also performed. Simulations were carried out in a two dimensional domain, under the hypothesis of laminar flow, and taking into account the thermal radiation by the solids boundaries (but not the participating fluid medium). An experiment, reproducing a rectangular cavity containing a regular distribution of cylindrical obstacles, was used to validate the

numerical solver for humidified and non-humidified air. The general features of flow were well predicted, while the model used was not able to correctly reproduce the local features of the flow, temperature and humidity. Das and Reddy [9] focused on the analysis of heat and air-flow in a two-dimensional cavity with two differentially heated walls, two insulating walls and a central square solid body. Conduction and convection phenomena were investigated changing the conductivity of substances, the Rayleigh numbers, and the inclination of the cavity.

Water change of phase also influences the system thermodynamics. Evaporation/condensation on solid surfaces absorbs/releases heat; in a wide range of applications these effects strongly alter the temperature at the solid boundaries. To obtain reliable results, the thermal interaction between the two media has to be simulated. This problem is referred in literature as conjugate heat transfer (CHT). Dorfman and Renner [11] presented a review of the approaches employed to face this problem. A detailed description of the main coupling strategies can be found in the work of Duchaine *et al.* [12],[13], who also analysed the numerical stability and efficiency of the coupling algorithms. Sosnowski *et al.* [31] proposed a Neumann-Neumann thermal coupling technique, that was used in Cintolesi *et al.* [7] for studying the turbulent natural convection in a square cavity with conductive boundaries.

As already highlighted, systems with natural convection, evaporation and condensation are characterised by high degree of complexity. Many physical phenomena can interact among them and drastically influence the flow field. However, the factors that mainly affect these systems in practical applications are: (i) turbulence; (ii) heat exchange between solid/fluid media; (iii) thermal radiation with participating fluid. The latter becoming more important as the humidity content increases.

In the present work we study evaporation and condensation processes from a solid body in a enclosure, at an applicative scale, representative, for example, of home appliances. Among the others, a dishwasher during the drying phase, evaporation from food in a oven, condensation in a fridge. The numerical model retrieves all the relevant physical features of such processes: turbulence is treated by means of a dynamic Lagrangian Large-Eddy Simulation (LES) methodology, ref. [23], which is suitable to deal with the complex geometry of a real device; buoyancy force, triggered by temperature and humidity differences, is considered by means of the Boussinesq approximation; evaporation and condensation processes are modelled through a specific boundary conditions, allowing for a simplified treatment of the water film, for the temperature and humidity equations; the heat can be transferred from solid to fluid domains (or *vice versa*) taking into account the latent heat due to evaporation (condensation). The inclusion in the model of the radiative thermal effects is in progress and will be included in a successive study.

The paper is organised as follows: section 2 describes the enclosure and supplies details on the case geometry;

section 3 presents the mathematical model and the numerical methodology adopted for simulations; section 4 describes the computational mesh and the simulation settings; in section 5 the results are reported and discussed; in section 6 we give concluding remarks.

2. Problem description

The case geometry, reported in Figures 1 and 2, is composed of a cubic domain of edge 0.75 m surrounded by a narrow metallic coat (the enclosure) and containing a rectangular plate (the plate). Among the possible industrial devices, it may be representative of a simplified dishwasher. The simulation is three-dimensional and periodic conditions are used in the z -direction, that is of homogeneity. Thus, the statistics can be collected along the spanwise direction since, on average, the flow develops on the $x - y$ plain. The enclosure is composed of mild steel sheets of thickness $H_e = 0.0015\text{ m}$. The plate is a solid rectangle with a vertical section of $H_p \times L_p = 0.005\text{ m} \times 0.25\text{ m}$, located at the middle of the cavity.

The scenario investigated is the following: the external enclosure is colder than the internal plate; both are wet by a thin water film. The humid air is driven by thermal and vapour gradients. As time goes on, water evaporates from the plate, cooling it down. In the meantime, air becomes more humid and the vapour condensates over the enclosure.

The evaporation and condensation processes are investigated for different materials of the internal plate. A detailed description of the simulation setting is given in section 4.3, while the mathematical and numerical models adopted are described in the following section.

3. Mathematical model

In the following, the subscripts are used to specify the different usage of variables. If ϕ represents a generic variable, then: ϕ_a is the variable related to air; ϕ_s is related to solid; ϕ_ω is related to vapour concentration; ϕ_0 is the variable reference value; ϕ_{SGS} is related to sub-grid-scale quantities.

3.1. Governing equations

Different physical phenomena have to be modelled by a suitable set of mathematical equations: natural convection in fluid domain, boundary heat exchange between solid and fluid media, vapour diffusion and water evaporation/condensation above the solid surfaces. They strongly interact on the solid-fluid boundaries, over which the heat transfer between media takes place, along with the release/absorption of latent heat by water condensation/evaporation, and the mass transfer between the liquid and vapour phase. Moreover, there buoyancy force peaks and triggers turbulence fluctuations.

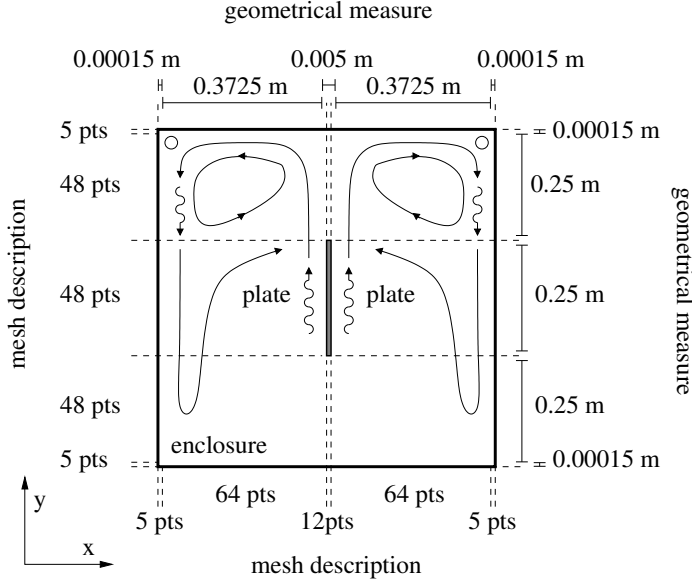


Figure 1: Schematic of the case investigated: the square cavity is filled with a mixture of air and vapour, it contains a hot internal plate and is surrounded by an external cold enclosure. In the cavity interior, the main initial fluid flow is sketched; geometrical information are on the top and right side; mesh grid information are on the bottom and left side.

The air flow is governed by the Navier-Stokes equations. The Boussinesq approximation, that includes the contribution of both temperature gradient and vapour concentration, is used for the buoyancy forces:

$$\frac{\partial u_i}{\partial x_i} = 0, \quad (1)$$

$$\frac{\partial u_i}{\partial t} + u_j \frac{\partial u_i}{\partial x_j} = -\frac{1}{\rho_0} \frac{\partial p}{\partial x_i} + \nu \frac{\partial^2 u_i}{\partial x_j \partial x_j} - \frac{\rho}{\rho_0} g \delta_{i2}, \quad (2)$$

$$\frac{\rho}{\rho_0} = 1 - \beta_T (T - T_0) - \beta_\omega (\omega - \omega_0), \quad (3)$$

where u is the fluid velocity, p is pressure, T is temperature, ρ is space-time variable density in the fluid flow, ω is vapour concentration. The zero subscript denotes the reference value of the corresponding variable.

The vapour concentration is defined as

$$\omega = \frac{m_v}{m_a + m_v}, \quad (4)$$

in which m_v and m_a are the vapour and air masses, respectively.

Temperature and vapour concentration in fluid medium are both modelled as active scalars. They are diffused and transported with air according to the advection-diffusion equations:

$$\frac{\partial T_a}{\partial t} + u_j \frac{\partial T_a}{\partial x_j} = \alpha_a \frac{\partial^2 T_a}{\partial x_j \partial x_j} + S_a, \quad (5)$$

$$\frac{\partial \omega}{\partial t} + u_j \frac{\partial \omega}{\partial x_j} = \alpha_\omega \frac{\partial^2 \omega}{\partial x_j \partial x_j}, \quad (6)$$

where S_a represents the heat source, due to vapour condensation.

Temperature diffusion in solid media is ruled by the classical equation of diffusion

$$\frac{\partial T_s}{\partial t} = \alpha_s \frac{\partial^2 T_s}{\partial x_j \partial x_j} + S_s \quad (7)$$

including the evaporation sink term S_s , that has to be modelled.

The wetting layer is not solved directly, rather it is modelled under the thin film assumption: H is a scalar representing the film thickness at the boundary and its evolution equation is derived from a suitable mass balance:

$$\frac{\partial H}{\partial t} = \frac{\rho_a}{\rho_w} U_\omega, \quad (8)$$

where ρ_a is the air density, ρ_w is the water density and U_ω is the evaporation/condensation velocity magnitude. Following ref. [25], the value $\rho_a/\rho_w = 0.001$ is adopted in our numerical simulations. If the gas is made of a binary mixture in which the two species are not soluble (like air and vapour), the evaporation/condensation velocity can be estimated by

$$\mathbf{U}_\omega = -\frac{\alpha_\omega}{1 - \omega_\Gamma} \left(\frac{d\omega}{dn} \Big|_\Gamma \right) \mathbf{n}, \quad (9)$$

where the subscript Γ indicates that the quantities are evaluated at the solid-fluid interface, n is the wall normal direction, while \mathbf{n} is the wall normal versor through the fluid domain. In literature such estimation is referred to as the *semi-impermeable* model (cf. Petronio [25] and Welty *et al.* [35]).

In order to solve equation (9), the value of vapour concentration at the interface Γ is required. It can be computed by:

$$\omega_\Gamma = \frac{M_v}{M_a} \frac{p_{sat}(T_\Gamma) \phi_\Gamma}{\left[p_{atm} - \left(1 - \frac{M_v}{M_a} \right) p_{sat}(T_\Gamma) \phi_\Gamma \right]}, \quad (10)$$

where $M_a = 28.97 \text{ g/mol}$ and $M_v = 18.02 \text{ g/mol}$ are the values of molar mass of air and water vapour respectively; p_{atm} and p_{sat} are the vapour atmospheric pressure at actual and at saturation condition (respectively); ϕ is the relative humidity evaluated at interface by:

$$\phi_\Gamma = \frac{P}{p_{sat}(T_\Gamma)}, \quad (11)$$

with P the equilibrium vapour pressure. If the wall is wet, $\phi_\Gamma = 1$ is assumed. At the atmospheric pressure of $p_{atm} = 101325 \text{ Pa}$, the *Buck's equation* provides an evaluation formula for saturation pressure, that reads:

$$p_{sat}(T) = 611.85 \exp \left[\frac{17.502 (T - 273.15)}{240.9 + (T + 273.15)} \right]. \quad (12)$$

Note that this expression is strictly valid for water-air interface.

The last term that has to be defined is $S_{a/s}$, the heat source or sink due to the water phase change. Water evaporation subtracts energy from the system, whereas condensation releases it. These energy exchanges occur onto the air/solid interface, and can be expressed as a boundary heat flux vector:

$$\mathbf{q}_{evap/cond} = \rho^* L_h \mathbf{U}_\omega, \quad (13)$$

where $\rho^* = \rho_a + \rho_v$ and ρ_v is the vapour density, $L_h = 2.26 \times 10^6 \text{ J/kg}$ is the latent heat of vaporisation (also called *enthalpy of vaporisation*). The value $\rho^* = 1 \text{ kg/m}^3$ is adopted, as recommended by Petronio [25], and L_h is considered constant throughout the process.

The heat flux vector is used to compute the temperature source/sink term, that is numerically applied to the first cell next to the boundary. When condensation occurs air is heated, thus the source term S_a in equation (5) is non-zero while $S_s = 0$ is imposed. Conversely, when evaporation occurs the solid is cooling, so the sink term S_s in equation (7) is non-zero while $S_a = 0$ is imposed. The source/sink term represents the energy stored in a cell, therefore it is computed as:

$$S_{a/s} = -\frac{\rho^* L_h}{(\rho C_p)_{a/s}} \nabla \cdot \mathbf{U}_\omega, \quad (14)$$

that is the divergence of the heat flux, divided by the heat capacity at constant pressure of the medium. Strictly speaking, equation (14) is not mathematically well defined, since \mathbf{U}_ω is defined by (9) just at the solid-fluid interface. The symbol \mathbf{U}_ω represents here the zero-extension of the evaporation/condensation velocity field to fluid domain: \mathbf{U}_ω is computed by (9) on the solid-fluid interface, while it is set to be the zero-vector elsewhere.

In this study, the water film is considered in thermal equilibrium with air and solid media. In fact, adopting the thin film assumption, water onto the wet surface has a very short temperature diffusion time with respect to other system components.

The vapour transport equation (6) is provided with the Dirichlet condition (10) if boundaries are wetted, and switches to the Neumann condition

$$\left. \frac{d\omega}{dn} \right|_\Gamma = 0, \quad (15)$$

if the water film completely evaporates. The boundary condition (15) does not allow diffusive flux at the dry surfaces. The surfaces are considered dry when H decreases under a limit value. In that case, U_ω is forced to be zero and recondensation is not anymore allowed.

The temperature equations (5) and (7) are provided with suitable boundary condition that accounts for the CHT at solid/air interface Γ . Thermal coupling boundary condition enforces the continuity of temperature and the balance of the heat fluxes:

$$T_s|_\Gamma = T_a|_\Gamma \quad (16)$$

$$k_s \left(\frac{\partial T_s}{\partial n} \right) = k_a \left(\frac{\partial T_a}{\partial n} \right) \quad (17)$$

where k is the thermal conductivity. More details on the coupling methodology herein employed can be found in Sosnowski *et al.* [31].

3.2. Large-eddy simulation methodology

In order to numerically solve the governing equations, a LES approach is adopted. Among the others, we refer to Sagaut [29] and Piomelli [26] for an introduction on this subject. The mesh implicit filter is applied to the equations of motion (1,2,3), to fluid temperature equation (5) and to vapour concentration equation (6), leading to the following Sub-Grid Scale (SGS) extra terms, respectively:

$$\frac{\partial}{\partial x_i} \tau_{ij} = \frac{\partial}{\partial x_i} (\overline{u_i u_j} - \overline{u_i} \overline{u_j}) \quad (\text{SGS stress tensor}) \quad (18)$$

$$\frac{\partial}{\partial x_i} h_i = \frac{\partial}{\partial x_i} (\overline{T_a u_i} - \overline{T_a} \overline{u_i}) \quad (\text{SGS heat flux}) \quad (19)$$

$$\frac{\partial}{\partial x_i} \lambda_i = \frac{\partial}{\partial x_i} (\overline{\omega u_i} - \overline{\omega} \overline{u_i}) \quad (\text{SGS vapour flux}) \quad (20)$$

where the bar indicates the filtered quantities.

The governing equations are closed with the dynamic Lagrangian SGS model, described by Meneveau *et al.* [23] and extended to active scalars by Armenio and Sarkar [4]. First, the Smagorinsky model is used for deviatoric part of stress tensor

$$\tau_{ij} - \frac{\delta_{ij}}{3} \tau_{kk} = -2\nu_{\text{SGS}} \overline{S_{ij}}, \quad (21)$$

and for the heat and vapour fluxes

$$h_i = -\alpha_{a,\text{SGS}} \frac{\partial \overline{T_a}}{\partial x_i}, \quad \lambda_i = -\alpha_{\omega,\text{SGS}} \frac{\partial \overline{\omega}}{\partial x_i}, \quad (22)$$

where $\overline{S_{ij}} = (1/2)[(\partial \overline{u_i}/\partial x_j) + (\partial \overline{u_j}/\partial x_i)]$ is the strain rate tensor; ν_{SGS} is SGS viscosity; $\alpha_{a,\text{SGS}}$ is SGS thermal diffusivity; $\alpha_{\omega,\text{SGS}}$ is SGS vapour diffusivity. Second, the SGS quantities are computed cell by cell, using the information from the resolved scales of motion. The details on the mathematical formulation of this model can be found in Cintolesi *et al.* [7] and they are not here reported.

3.3. Numerical approach

Simulations are carried out using a home-made solver, developed within the framework of OpenFOAM. This is an open source software package, written in C++, for computational fluid dynamics.

The fluid solver is based on the Pressure-Implicit with Splitting of Operation (PISO) algorithm, and uses the finite volume method. The governing equations are discretised through a second-order central difference scheme in space, and a backward difference in time, thus ensuring an overall accuracy at the second order.

The overall resolution algorithm is now briefly summarised: first, the temperature equation is solved for all domains (fluid and solid); second, the equation for vapour concentration is solved in the fluid domain, followed by

the Navier-Stokes equations; third, temperature sub-loop starts and performs the thermal coupling between solid-fluid domain taking in account the thermal contribution of evaporation and condensation; fourth, the vapour equation is solved again and the water film thickness is calculated.

In order to ensure a better numerical stability during the thermal coupling computation (third step), the heat flux due to evaporation and condensation (13) is not directly imposed as boundary condition. Instead, the already explained strategy (add the temperature source/sink term (14) on the first cell next to the boundary) is adopted. The latter approach is preferred because it has been found to be more stable than to the former.

More details on the numerical implementation of thermal coupling and evaporation-condensation models can be found in Sosnowsky [30] and Petronio [25], respectively.

The inversion techniques used are: for pressure, preconditioned conjugate gradient (PCG in OpenFOAM notation) solver for symmetric matrices, using a simplified diagonal-based incomplete Cholesky (DIC) preconditioner; for others variables, preconditioned bi-conjugate gradient (PBiCG) solver for asymmetric matrices, using the simplified diagonal-based incomplete LU (DILU) preconditioner. For all the variables the residual tolerance is 10^{-8} . The implementation details on these basic solver can be found in the official documentation of the code, ref. [1, 2].

4. Simulation settings

The settings and the physical assumptions adopted for the problem described in section 2, are illustrated hereafter, along with the non-dimensional numbers governing the system.

4.1. Non-dimensional parameters

The parameters related to the thermal-solute convection are: the total Rayleigh number, that characterises the buoyancy-driven flows

$$Ra = \frac{g\beta_T \Delta T L^3}{\nu\alpha_a} + \frac{g\beta_\omega \Delta\omega L^2}{\nu\alpha_\omega}, \quad (23)$$

composed by the sum of thermal and solute contributions. It can be interpreted as the ratio between the destabilising effect of buoyancy forces and the stabilising effect of momentum and thermal diffusion.

The total Grashof number, that also includes a thermal and a solute contribution

$$Gr = \frac{gL^3}{\nu^2} (\beta_T \Delta T + \beta_\omega \Delta\omega), \quad (24)$$

is the ratio between the buoyancy and viscous forces.

The characteristic temperature diffusion time in a solid medium

$$\tau = \frac{\ell^2}{\alpha_s}, \quad (25)$$

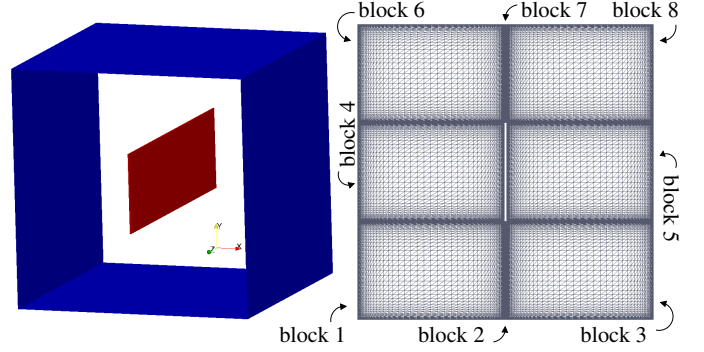


Figure 2: Sketch of the cavity-plate case: left, a three dimensional overview of the cavity; right, z -normal section of the mesh for fluid domain.

which gives the time-scale needed by the solid to conduct temperature along a distance ℓ .

The characteristic velocity for bounded flows dominated by buoyancy force, defined as

$$U_0 = \sqrt{(\beta_T \Delta T + \beta_\omega \Delta\omega)gL}, \quad (26)$$

where L is the length scale of the system. The time scale is computed as $t_0 = L/U_0$.

For the problem under consideration we set: $\Delta T = (T_p - T_e) = 50 K$ the initial difference of temperature between the plate and the enclosure; $\Delta\omega = \omega_\Gamma(T_p) - \omega_\Gamma(T_e) = 0.1255$ the initial difference of vapour concentration at plate and enclosure surface; $L = 0.375 m$ the characteristic length (half of the cavity edge).

With these choices, the preliminary simulation is characterised by a global Rayleigh number of $Ra = Ra_T + Ra_\omega \simeq 5 \times 10^8$, a Grashof number of $Gr \simeq 5 \times 10^8$ and a characteristic velocity of $U_0 = 0.95 m/s \simeq 1 m/s$.

The variables are made non-dimensional as: length $x/2L$; time t/t_0 ; temperature $(T - T_e)/\Delta T$; velocity u_i/U_0 ; vapour concentration ω/ω_{asy} ; water film thickness H/H_i .

4.2. Computational grid

The three elements composing the case (fluid, external enclosure, internal plate) are discretised with different meshes.

The fluid domain is discretised with a multi-block grid. The block dimensions are reported in Figure 1 and the mesh structure is sketched in Figure 2. The eight blocks composing the mesh are stretched near the walls with a double-side stretching function, based on hyperbolic tangent:

$$r(\xi) = \frac{1}{2} \left(1 + \frac{\tanh(\delta(\xi - 1/2))}{\tanh(\delta/2)} \right). \quad (27)$$

where ξ are the coordinates of equispaced partition. Different stretching factor δ are used for vertical (δ_y) and

horizontal (δ_y) directions. The grid is stretched in such a way that the cells at the interface between two blocks have the same dimensions. The narrow blocks (number 2 and 7 in Figure 2) are discretised using $12 \times 48 \times 64$ points, with stretching factors $\delta_x = 6$ and $\delta_y = 5$. The other blocks are discretised with $48 \times 48 \times 64$ points and a stretching factors of $\delta_x = \delta_y = 5$. The mesh stretching ensures at least 8 – 10 computational nodes within $y^+ \leq 10$ near the vertical and horizontal walls (for the preliminary simulation that is presented in Section 4.3).

The enclosure mesh is built in a similar manner, in a way to ensure the same cell dimensions at the fluid-enclosure interface. Along the interface, the mesh follows the structures of the fluid domain blocks; at the interface normal direction, the steel sheets are discretised with 5 points.

The plate mesh is the same of the fluid narrow blocks, in order to ensure the same cell dimensions on fluid interface. Thus the grid is composed of $12 \times 48 \times 64$ points with stretching factors $\delta_x = 6$ and $\delta_y = 5$.

4.3. Boundary and initial conditions

First, a simplified preliminary case is run, in order to provide an univocal initial configuration for the drying-process cases described in Section 2.

In the preliminary case, the enclosure and the plate have an uniform internal temperature of $T_e = 283.15\text{ K}$ and $T_p = 333.15\text{ K}$, respectively. The CHT is switched-off and replaced by a constant temperature condition on the solid faces. Therefore, the temperature of the solid media is not allowed to change. The fluid starts from rest and the no-slip condition is set on the solid boundaries. A water film of thickness $H_i = 0.0001\text{ m}$ wets the faces of the plate and of the enclosure. The film thickness is held constant, even if the water is allowed to evaporate and condensate. The physical parameters used for air and vapour are listed in Table 1. Along the spanwise direction, periodic conditions are set for all variables. The simulation time-step dt is computed at each iteration to guarantee that the maximum Courant number is $Co = dt|\bar{\mathbf{u}}|/\delta x \leq 0.5$; where $|\bar{\mathbf{u}}|$ is the velocity magnitude through the cell and δx is the cell size in the direction of the velocity.

The absence of thermal coupling and the presence of an inextinguishable water film, allows to reach a statistical steady state configuration (*i.e.* the fluid flow regime such that statistics are converged in time, meaning that they do not change with the variation of the time windows over which they are calculated). In such configuration, the rate of evaporation from the plate is balanced by the rate of condensation on the enclosure, and the fluid domain results saturated of vapour.

The preliminary simulation is run for a time interval sufficient to fully develop the fluid motion. The simulation is considered at statistical steady state when the volume-average value of vapour concentration within the fluid domain remains constant in time. Starting from a dry air condition ($\omega = 0$), vapour concentration reaches

Air		
ν	$[m^2/s]$	1.568×10^{-5}
α_a	$[m^2/s]$	2.220×10^{-5}
$(C_p)_a$	$[J/(kg \cdot K)]$	1.005×10^3
ρ_a	$[kg/m^3]$	1.165
k_a	$[W/(m \cdot K)]$	0.026
β_T	$[1/K]$	3.300×10^{-3}
Vapour		
α_ω	$[m^2/s]$	3.29×10^{-5}
ρ^*	$[kg/m^3]$	1
β_ω	–	0.63
L_h	$[J/kg]$	2.26×10^6
ρ_w	$[kg/m^3]$	1×10^3

Table 1: Physical parameters used in this study of air and vapour at 303.15 K (30°C), atmospheric pressure.

the asymptotic average value $\omega_{asy} = 0.025$ after roughly $\Delta t = 360t_0$ (more than two minutes of physical time).

The boundary conditions for drying-process simulations are the same as those of the preliminary one, but the CHT is switched on over the solid faces in contact with air. The adiabatic condition (zero temperature gradient) is imposed at the external enclosure surfaces. Also, the water film is now allowed to change its thickness according to equation (8). Three drying-process simulations are performed changing the material of the internal plate, while the external enclosure is always made of mild steel. The materials used are listed in Table 2, together with their thermal properties.

The materials are chosen to be representative of three main classes, respectively that of good thermal insulator (PVC), intermediate thermal insulator (porcelain), and good thermal conductor (mild steel). Such materials are samples of three categories of high/low conductivity k and high/low heat capacity ρC_p . In principle, a fourth category exists having high k and low ρC_p , but ordinary materials do not have these characteristics, thus it is not considered in this study. A detailed discussion on these thermal categories can be found in Cintolesi *et al.* [7].

5. Results and discussion

To the knowledge of the authors, no experimental or numerical results are available for a validation of the present (or similar) case.

The numerical solver was previously tested in all its parts: the evaporation and condensation process was successfully validated against different benchmark cases by Petronio [25]; the thermal coupling implementation was tested in the work of Sosnowski *et al.* [31]; the accuracy of the flow solver and of the turbulent model were verified

MATERIAL		PVC	Porcelain	Steel
C_p	$[J/(kg \cdot K)]$	900	750	500
ρ	$[kg/m^3]$	1300	260	7830
k	$[W/(m \cdot K)]$	0.19	2.20	45.30
$\rho C_p \times 10^{-3}$	$[J/(m^3 \cdot K)]$	1170	195	3915
$\alpha_s \times 10^5$	$[m^2/s]$	0.016	1.130	1.160
$\tau_{ver} \times 10^{-3}$	$[s]$	390.62	5.53	5.38
τ_{hor}	$[s]$	156.25	2.20	2.20

Table 2: Thermal physical properties of materials used for drying-process simulation. Data taken from ref. [3], except for data of *Poly Vinyl Chloride* (PVC) taken from ref. [31].

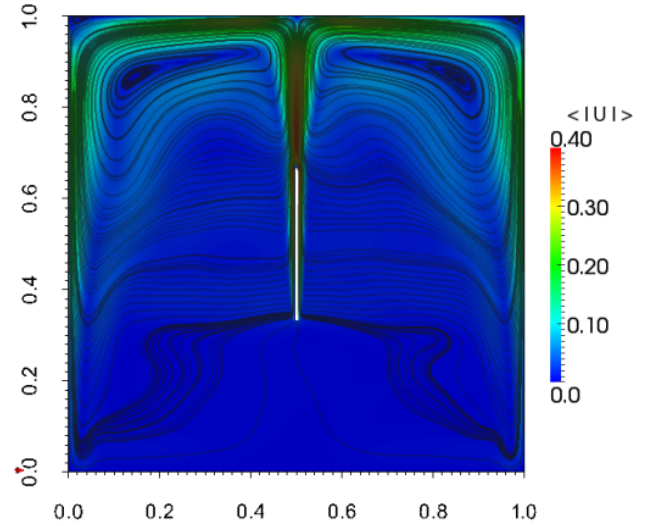
in the former numerical investigation on turbulent natural convection in square cavity at $Ra = 1.58 \times 10^9$, ref. [7].

Special care have been taken setting the spatial and temporal discretisation of the simulations. Ref. [7], where an extensive tests on the quality of the results were performed, is taken as reference for the present case. The analysis reported in the Appendix of that paper, shows that the grid size used was able to accurately reproduce the flow statistics. The grid stretching near the solid walls ensured a direct computation of the flow boundary layer, while the high stretching employed did not influence the dynamical computation of turbulent SGS stresses. Moreover, the choice of the time step did not affect the quality of results, when the Courant number is $Co < 1$.

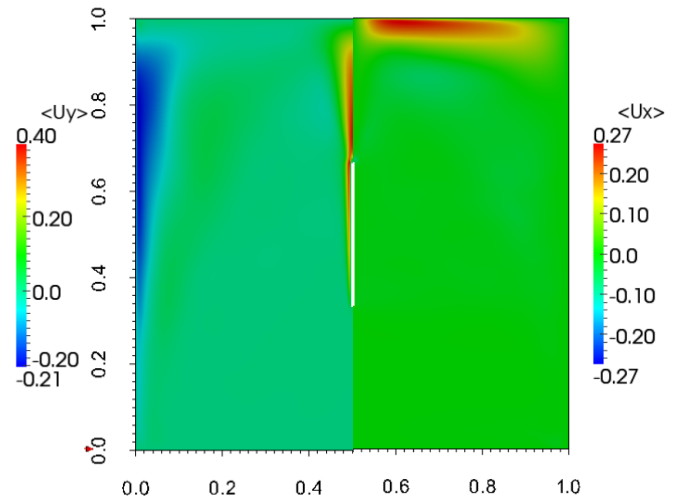
The Rayleigh number of the present study is $Ra = 5 \times 10^8$ for the preliminary simulation (smaller for the others). It is lower than that of the reference investigation [7]. The computational grid of the present simulation has an analogous structure and the same wall stretching of the reference one, still being used for a less demanding value of Ra . The constrain of $Co \leq 0.5$ is assumed to be adequate, since in the reference simulation the results were nearly insensitive to the variation of this parameter when it is lower than 1. The computational domain in the homogeneous direction is chosen large enough to ensure the development of the largest turbulent scales. The autocorrelation functions are checked for the final configuration of the preliminary simulation. It is found that autocorrelations decay to small values. This suggests that the domain z -direction is large enough to allow the use of periodic condition. Hence, the computational set-up employed in the present study has to be considered adequate to accurately resolve the fluid flow structures.

5.1. Preliminary simulation

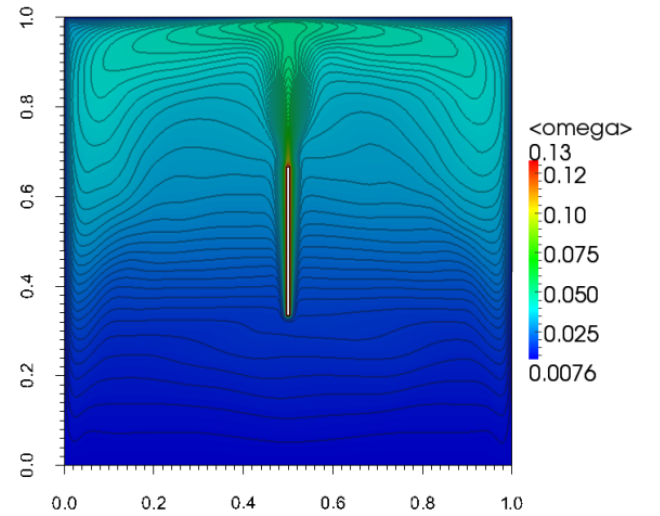
The results of the preliminary simulation are now discussed. In this section the angular brackets indicate the average in time and in the spanwise direction. The time average is computed over a period of $13 t_0$ (corresponding to 5s of physical time), after that the statistical steady state has been reached.



(a) Streamlines of the average velocity $\langle \mathbf{u} \rangle$.



(b) Distribution of velocity components over the fluid domain: left, the vertical component $\langle u_y \rangle$; right, the horizontal component $\langle u_x \rangle$.



(c) Contour plot of average vapour concentration $\langle \omega \rangle$.

Figure 3: Mean flow, thermal field and vapour concentration for the preliminary simulation.

Figure 3 displays the spatial distribution of mean quantities. For all flow variables, the system is symmetric with respect to the vertical centre-line; thus, hereafter the right side of the cavity is discussed.

In Figure 3a the velocity magnitude contour plot is shown along with the flow streamlines, while Figure 3b depicts the distribution of the velocity components in the cavity. The flow is driven by the buoyancy force arising in correspondence of the hot plate and the vertical cold enclosure walls. It is qualitatively sketched in Figure 1. The main stream is localised near the boundaries and three zones of high speed motion can be identified in Figure 3b, namely:

Ascending region: is a thin vertical plume with width as large as that of the plate, extending approximately in the range $0.65 \lesssim y/2L \lesssim 0.95$. It is generated by the air blowing up from the hot vertical plate. The vertical velocity here is at its climax, that is estimated to be $|U|_{max} \simeq 0.4 \text{ m/s}$.

Horizontal-flow region: is located along the ceiling (the enclosure horizontal top wall), between $0.55 \lesssim x/2L \lesssim 0.90$ and $0.95 \lesssim y/2L \lesssim 1$. In this zone, the main stream loses velocity and air flows towards the vertical cold wall of enclosure. The contact with ceiling decreases the air temperature and allows corner-flow separation and a recirculation vortex is generated in the top corner;

Descending region: is a triangular-shaped zone, with the two sides extending in the ranges $0.25 \lesssim y/2L \lesssim 0.95$ and $0.90 \lesssim x/2L \lesssim 1$ respectively. Hot air reaches the cold vertical wall, and the buoyancy force is triggered by the high temperature difference pushing air downward.

Outside these regions, the fluid motion is less intense. The upper-half cavity ($0.5 \gtrsim y/2L$) is characterised by a diagonal-flow that drives air from the descending to the ascending region. This flow is sensibly weaker than the others previously described. Between the diagonal-flow and the horizontal-flow region, a stable recirculation vortex is generated. It is elongated along the horizontal direction and the centre is located approximately on the square off-diagonal at $c = (0.85, 0.85)$ in non-dimensional units. In the bottom-half cavity ($0.5 \lesssim y/2L$), far from the vertical walls, air is almost at rest. Figure 3c displays the contour plot of vapour concentration. The contour plot of temperature is similar, thus it is not reported. This is expected: in absence of CHT, the source term in equations (5) and (6) disappears. Hence, T and ω are ruled by similar equations, both provided with Dirichlet boundary conditions, and with similar diffusion coefficients (cf. Table 1). We limited our attention to ω ; analogous considerations can be done for temperature.

Fluid domain is strongly stratified: the larger amount of vapour is localised in the upper-half of the cavity, while

the bottom-part is characterised by a homogeneous low concentration of vapour.

The horizontal centreline ($y/2L = 0.5$) sharply separates the two regions. Vapour reaches the maximum in the proximity of the hot plate (as a result of the strong evaporation process) and in the ascending region. Humidity is transported by the flow, therefore high value of ω can be found in the horizontal-flow region and in the descending region.

The top corner region is characterised by a lower vapour concentration due to the fact that this region is separated by the main flow, since the corner vortex creates a sort of relative dry air bubble. Condensation occurs when the ascending flow impinges the ceiling, and when air approaches the enclosure walls. A rapid reduction of vapour close to the cold boundaries is detected. The bottom-half of cavity is characterised by a homogeneous vapour distribution.

The asymptotic volume-average values $\omega_{asy} = 0.025$ is useful to check when the simulation arrived at steady state, but it cannot give any information about the local vapour concentration. Indeed, ω is strongly non-homogeneously distributed.

Velocity, temperature and vapour concentration profiles over a number of selected lines are presented in the following section 5.2.5, where they are compared with those of the drying-process simulations.

5.1.1. Comparison between dry and humid air cases

For the sake of completeness, an additional simulation is performed considering dry air: the same set-up as for the preliminary simulation is used, but air is not humid ($\omega = 0$) and the solid surfaces are dry. In such conditions the evaporation/condensation and vapour transport models are not active. The simulation is carried out for the same period of time as the preliminary one, and the statistics are collected following the same criteria.

The dry air case presents many analogies with the humid air one. The general flow dynamics and temperature distributions are similar to that ones shown in Figure 3; hence, they are not reported here.

Figure 4 shows the velocity components at three characteristic locations, for dry and humid cases. The fluid flow mainly develops near the solid boundaries. The two profiles are similar but the velocity peaks are lower for the dry air case: the drop of velocity peaks is in the range 18% – 15%, while the maximum value of velocity magnitude is 20% lower. Indeed, the vapour contribution in equation (3) generates a stronger buoyancy force in humid air case.

The temperature profiles of the two cases are not reported, since they practically collapse one over the other. This is expected because the thermal equilibrium is ruled by the isothermal boundary condition, and it has to be the same for both cases. The thermal profiles for the preliminary simulation are presented in Figures 12,13.

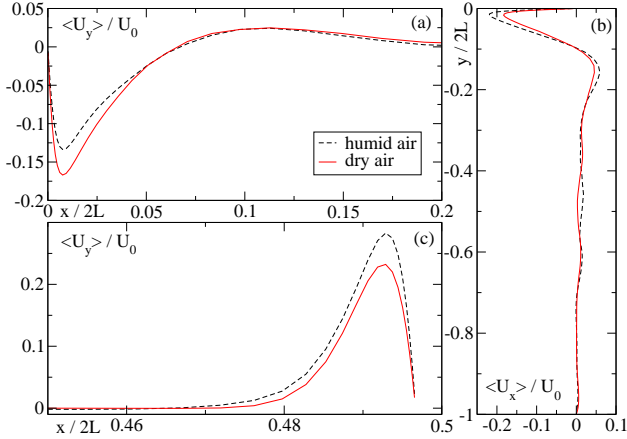


Figure 4: Averaged non-dimensional velocity components for dry and humid air simulations: (a) vertical velocity near the vertical enclosure wall, along the $y/2L = 0.5$; (b) horizontal velocity along a vertical line $x/2L = 0.25$; (c) vertical velocity near the vertical plate wall, along line $y/2L = 0.5$.

5.1.2. Heat transfer rate

The heat transfer due to conduction and convection (sensible heat flux) and water change of phase (latent heat flux) is here discussed. The two contributions are given by:

$$q_T = k \frac{dT}{dn} \Big|_{\Gamma} \quad (\text{sensible}); \quad (28)$$

$$q_\omega = \rho^* L_h U_\omega \quad (\text{latent}). \quad (29)$$

The heat fluxes for dry air and preliminary simulations are compared.

Figure 5 reports the sensible and latent heat transfer coefficients, respectively

$$h_T = \frac{q_T}{\Delta T} \quad \text{and} \quad h_\omega = \frac{q_\omega}{\Delta T}, \quad (30)$$

at three surfaces: (a) the ceiling, (b) the vertical plate and (c) enclosure walls. At the ceiling, the heat exchange is maximum where the plume of hot air generated at the plate impinges the enclosure. As expected, the higher heat transfer rate occurs at the plate surface: it is stronger in the bottom part of the plate, that is in contact with the cold air coming from the bottom part of the cavity. The latent flux peaks at the plate edges, where evaporation is particularly strong. At the enclosure vertical walls, a quasi-linear decreasing of fluxes along the y -direction can be detected. This is due to the fact the hot and humid air is concentrated in the top region of the cavity; conversely, it becomes colder and dryer when the bottom region of the cavity is approached.

The fluxes q_T are similar for the two cases, but in humid air case the latent heat flux dominates the heat transfer process. For humid air case, q_T is slightly higher when the q_ω has high values. In fact, the change of phase pro-

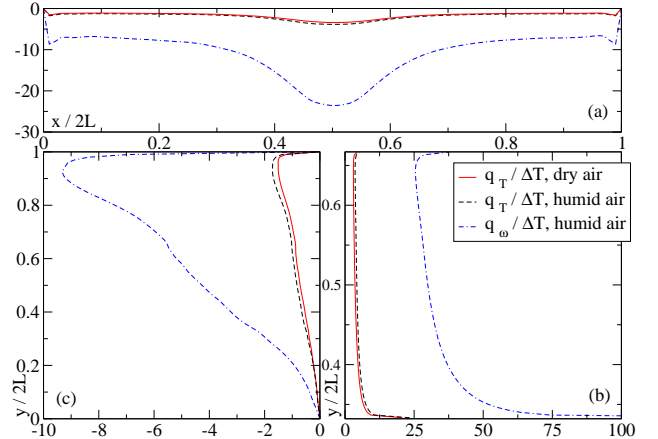


Figure 5: Averaged heat transfer coefficients for dry and humid air simulations: q_T is sensible heat flux; q_ω is latent heat flux. The fluxes are computed at the following surfaces: (a) enclosure ceiling; (b) vertical plate wall; (c) vertical enclosure wall.

cess increases the difference of temperature within the air, leading to a higher wall normal thermal gradient.

5.2. Drying-process simulations

The drying-process simulations are now discussed. In order to reach the final configuration (fluid at rest; constant vapour concentration; thermal equilibrium among enclosure, plate and air), a long physical time is required, eventually leading to huge simulation efforts.

All cases are run for about $\Delta t = 160t_0$, corresponding to 60s of physical time. At this time, the systems are still in a transitory phase. However, this period is meaningful to analyse the influence of the different plate materials on the overall thermal-solute dynamics.

5.2.1. Time evolution of global quantities

Figure 6 reports the main quantities involved in the evaporation/condensation process, averaged over suitable portions of domain. The average quantities could not be significant from a local point of view, because of the strong non-homogeneous distribution of the variables. However, they are useful to analyse the time evolution of the different simulations.

Figure 6a shows the time evolution of the non-dimensional temperature, averaged over the vertical surface of the plate. When CHT is active, evaporation subtracts heat from the plate. The process is ruled by equation (7) that, at the first cell near the solid surface, reads as:

$$\frac{\partial T_s}{\partial t} = \frac{k_s}{(\rho C_p)_s} \frac{\partial^2 T_s}{\partial x_j \partial x_j} - \frac{\rho^* L_h U_\omega}{\rho C_p}. \quad (31)$$

The sink term due to evaporation is balanced by the conduction term, that transports heat from the interior onto the surface of the plate. The heat transfer between solid and fluid introduces an additional sink of heat.

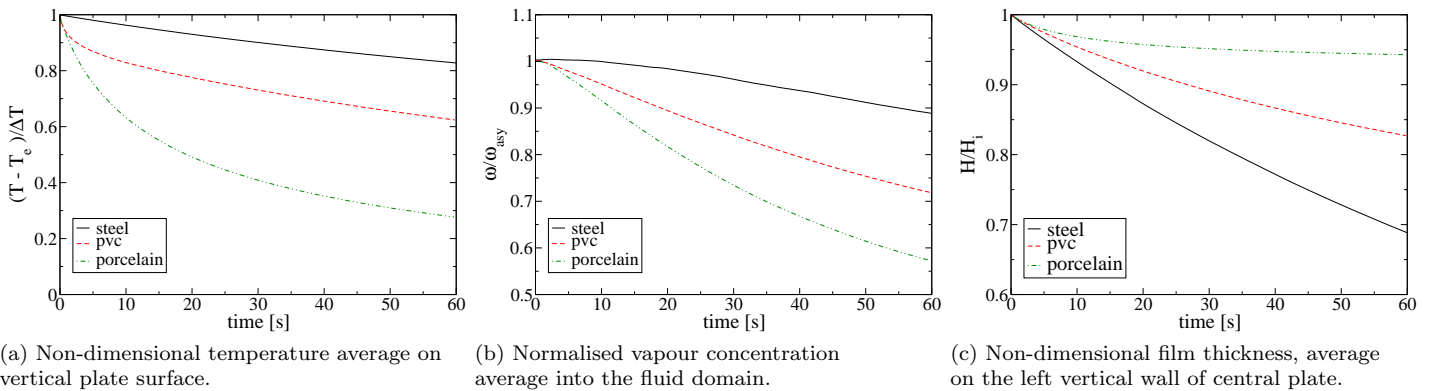


Figure 6: Global quantities for the drying-process simulations.

Overall, the heat transfer process is dominated by the evaporation sink term, because of the high value of the latent heat coefficient L_h . Steel plate experiences the lowest decrease of temperature: its high specific heat capacity ρC_p allows for smaller heat subtraction by evaporation. In this case temperature decreases almost linearly in time. PVC has an intermediate heat capacity. Initially it exhibits a high decrease of temperature, followed by an almost linear decrease. Porcelain has the lowest value of ρC_p , thus temperature has a strong non linear decay.

The floor (bottom horizontal enclosure wall) exhibits an almost negligible increase of temperature. The vertical walls and ceiling behave in an opposite way with respect to the plate (not shown): the mean surface temperature increases due to vapour condensation.

Figure 6b depicts the time variation of average vapour concentration in air, which is strictly related to the evolution of enclosure and plate temperatures. When CHT is switched on, the plate starts cooling down and evaporation is inhibited. In the meantime the enclosure is warmed up, leading to a reduction of condensation rate. The balance between the reduction of evaporation and condensation, determines the increase or decrease of mean vapour concentration.

In general, this rate is influenced by the thermal proprieties of the solid materials and by the enclosure. In our cases, it is crucial that the surfaces over which condensation occurs, are much more extended than the evaporating surfaces. Therefore, the quantity of water evaporated decreases (on average) much more than the water condensed and all cases exhibit a reduction of ω .

The differences among materials are related to their thermal inertia, since materials that maintain the plate hotter release more vapour in air: steel has a high level of vapour thanks to the higher plate temperature; PVC shows an almost linear reduction of ω ; porcelain has the faster decreasing due to the fast plate cooling and, hence, the higher reduction of water evaporation.

Figure 6c reports the average thickness of water film onto the vertical plate surface. The complete film con-

sumption process takes long time. This is due to the high level of vapour concentration in air that limits the evaporation rate. Up to the available simulation time, steel and PVC continue to reduce the film thickness, while porcelain basically reaches a steady condition and (on average) cannot allow for more evaporation than 5% of the water onto the plate.

5.2.2. Dew-point temperature estimation

In the previous Section, it was pointed out that porcelain is subject to a rapid cooling process. In order to understand if the phenomenon of vapour recondensation on the plate surface can occur, the dew-point temperature is here estimated.

The dew-point temperature is defined as the temperature at which humid air has to be cooled down to reach vapour saturation (at constant pressure and water content). A simple and well-known analytic form for the dew-point temperature T_{dp} is

$$T_{dp} = \frac{c \ln(P/a)}{b - \ln(P/a)}, \quad (32)$$

where P is the actual water vapour pressure that can be computed by equation (11), while a, b, c are empirical constants. Barenbrug [5] evaluates such constants as $a = 6.105$, $b = 17.27$, $c = 237.7$, if the air temperature is in the range $0^\circ C < T < 60^\circ C$. We refer to Lawrence [21] for a description and a derivation of equation (32).

Usually, an explicit expression of T_{dp} depending on temperature and relative humidity is derived, using the so called (*Magnus formula*) to evaluate the saturation pressure as a function of temperature. However, we are interested to a relation that involves surface vapour concentration ω_Γ instead of relative humidity.

Inverting equation (10) for the variable $P = p_{sat}(T_\Gamma) \phi_\Gamma$, we obtain:

$$P = \frac{\omega p_{atm}}{\frac{M_v}{M_a} + \omega \left(1 - \frac{M_v}{M_a}\right)}. \quad (33)$$

Substituting (33) in equation (32), we obtain an expression to estimate the surface dew-point temperature.

The average vapour concentration value, shown in Figure 6b, is used to compute T_{dp} in our drying-process cases. The dew-point temperature assumes low values ($T_{dp} < 287K$) during the entire time interval simulated. It goes under the minimum values T_e after about 30s for porcelain case. The other materials maintain (on average) higher plate temperature than the dew-point one during the simulations. Thus, vapour recondensation on the plate surface cannot take place.

5.2.3. General motion

Data analysis is carried out on the initial configuration $t = 0$ and on three intermediate configurations at times $t = 15, 30, 60 s$, corresponding to 25%, 50%, 100% of the total simulated interval, respectively. For each material, the intermediate configurations exhibit small changes among them, thus only the last is discussed.

The velocity streamlines and the T, ω contour plots for the final time $t = 160t_0$, are here discussed. The quantities are averaged in spanwise direction and in time, over an interval $\Delta t = 1s \simeq 2.5t_0$. The fluid flow is assumed to be homogeneous also in time during this short interval.

In Figure 7 the velocity streamlines are reported, together with the contour plots of velocity magnitude. The main flow exhibits a good symmetry with respect to the vertical centreline, except for the bottom part. In this region the flow is almost absent since the fluid is strongly stratified. Hence, the streamlines in the bottom-half cavity are not significant.

All cases maintain the main flow structures described in section 5.1; in particular the corner vortices and the recirculation vortices can be clearly seen. However, a general decrease of velocity magnitude can be observed.

In steel case, the velocity is higher than in the PVC one. Both cases show a flow field similar to that of the preliminary simulation: the recirculation vortices in the upper-half of the cavity are horizontally elongated, and the diagonal-flow maintains the curve trajectory (almost vertical near the vertical walls, deflecting on horizontal direction when approaching the ascending region). Porcelain case experiences the stronger velocity decay in the ascending region. Velocity field becomes comparable (in magnitude) among the three zones of motion beforehand described. The diagonal-flow does not show the vertical-horizontal behaviour described for steel and PVC, but has a straighter trajectory. The recirculation vortices are less horizontally elongated and follows the corner shape.

The velocity reduction is found to be proportional to the temperature drop. The velocity peak values at the end of simulations are reduced by: 85% for steel, 68% for PVC, 36% for porcelain with respect to the initial values. These values are, in general, well correlated with the drop of average temperature on the plate surface (reported in Figure 6a).

Figure 8 depicts the temperature contour plots. As expected, the behaviour of fluid temperature follows the variation of plate surface temperature. The steel case main-

tains a configuration similar to the initial one (not reported, ref. to Figure 3c): air is hot in the ascending and horizontal-flow regions, while it is cooled down near the vertical walls. The cavity is strongly non homogeneous and it is clearly divided into two parts: the upper-half has higher temperature, especially in the main flow regions; the bottom-half has a lower and more uniform temperature distribution. In the PVC case, the upper-half of the cavity is more homogeneous with respect to the steel case. A plume of hot air is only detected in the ascending region. A strong thermal stratification between the upper and bottom-half cavity is still visible. On the contrary, the porcelain case is affected by a strong cooling process. The fluid domain is characterised by a weak thermal stratification, with a low vertical temperature gradient.

Figure 9 reports the distribution of the non-dimensional vapour concentration. The general behaviour resembles that one of temperature. However, for all materials, ω decreases more rapidly than temperature. Comparing, for example, Figure 9c with 8c, it can be seen that the vapour concentration is almost uniform in vertical direction, while temperature exhibits a positive vertical gradient. When CHT is considered, the contour lines of vapour concentration and temperature are not anymore similar to each other, as it happens for the preliminary case. This is due to the different boundary conditions imposed: temperature undergoes CHT boundary conditions (16), (17) and is affected by the heat source/sink term (14); whereas ω is computed at the interface by (10). This latter is a monotone function that decreases rapidly with temperature. When the surface loses heat, the boundary conditions reduce more the vapour concentration than the temperature. From a physical point of view, when plate temperature decreases, both evaporation and heat transfer are reduced in the fluid. Evaporation decreases more rapidly than the thermal heat transfer, leading to a different ω distribution with respect to T .

5.2.4. Surface quantities

The distribution of temperature and water film over the solid body surfaces, is now discussed. For the three drying-process simulations, the scalars are sampled at different transitory stages; namely at time $t = 15, 30, 45, 60 s$ corresponding to 25%, 50%, 75%, 100% of the simulated period, respectively.

Figure 10 reports the non-dimensional temperature over the plate vertical centreline (upper panel), and the non-dimensional film thickness on the vertical plate surface (lower panel). In both cases the quantities are averaged along spanwise direction. The H profile on the plate left surface coincides with that one on the right surface, by virtue of system symmetry. Temperature is plotted over the plate centreline. Thermal conductors (steel and porcelain) show a negligible temperature variation between the surface and the centreline; except at the very beginning, when evaporation starts. The insulator (PVC) has a small temperature variation (3% maximum). Anyway, this ef-

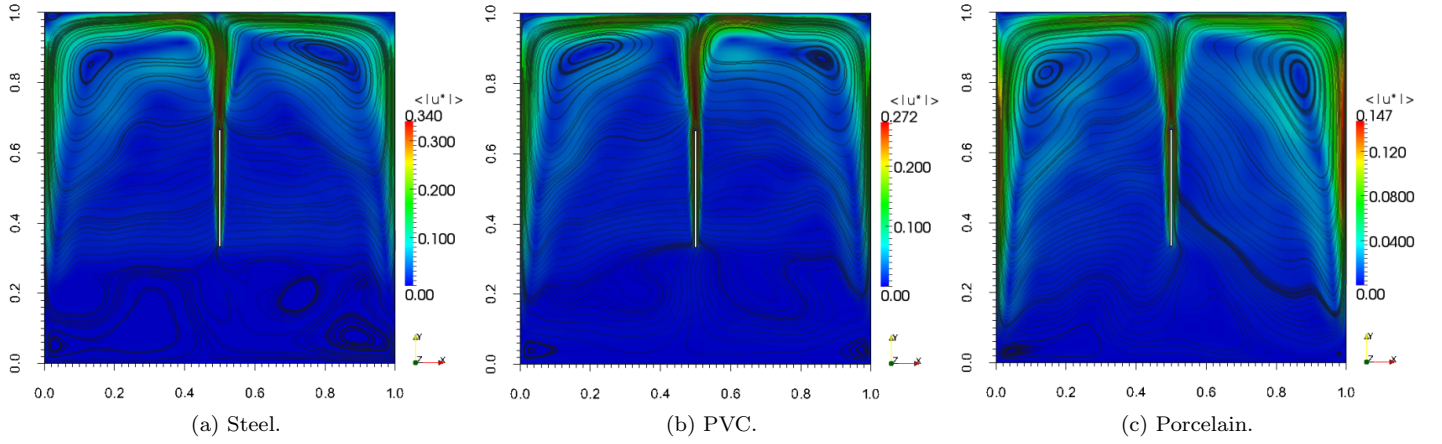


Figure 7: Velocity $\langle |\mathbf{u}^*| \rangle = \langle |\mathbf{u}/U_0| \rangle$ streamlines and magnitude for the final time configuration.

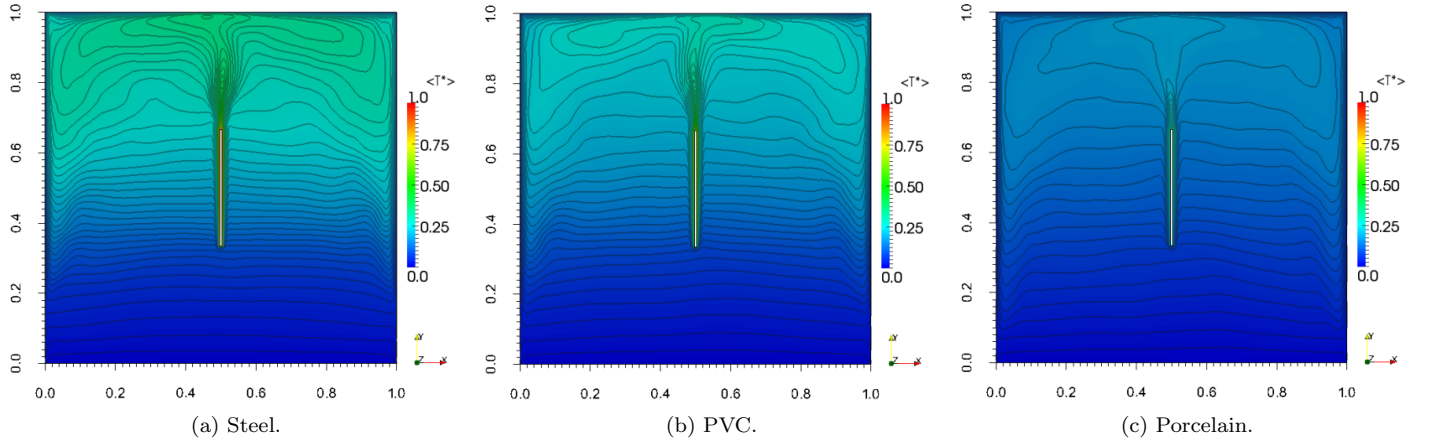


Figure 8: Non-dimensional temperature $\langle T^* \rangle = (\langle T \rangle - T_e)/\Delta T$ contour plot for the final time configuration.

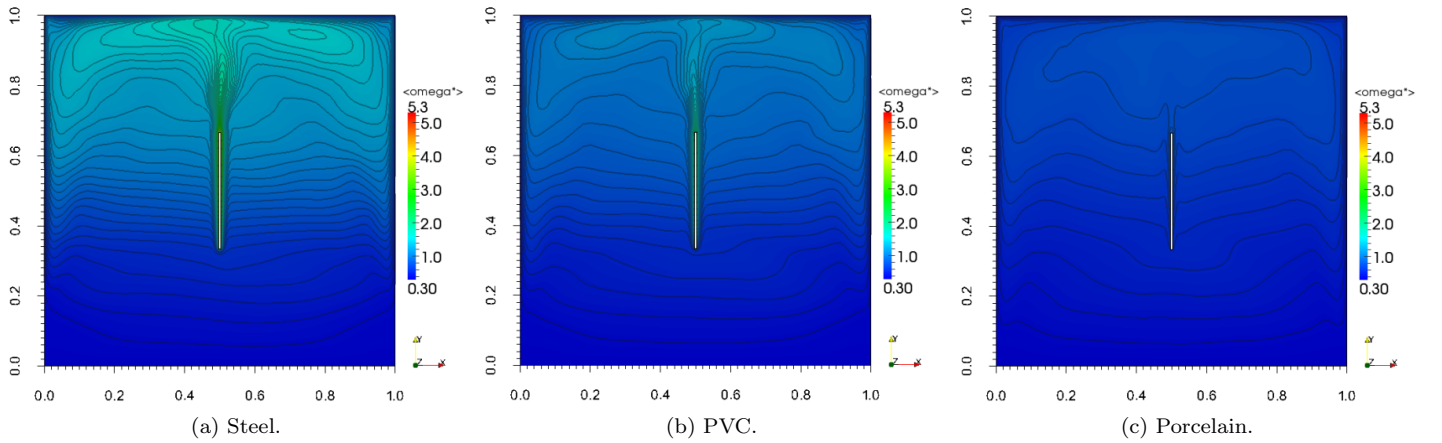


Figure 9: Non-dimensional vapour concentration $\langle \omega^* \rangle = \langle \omega \rangle / \omega_{asy}$ contour plot for the final time configuration.

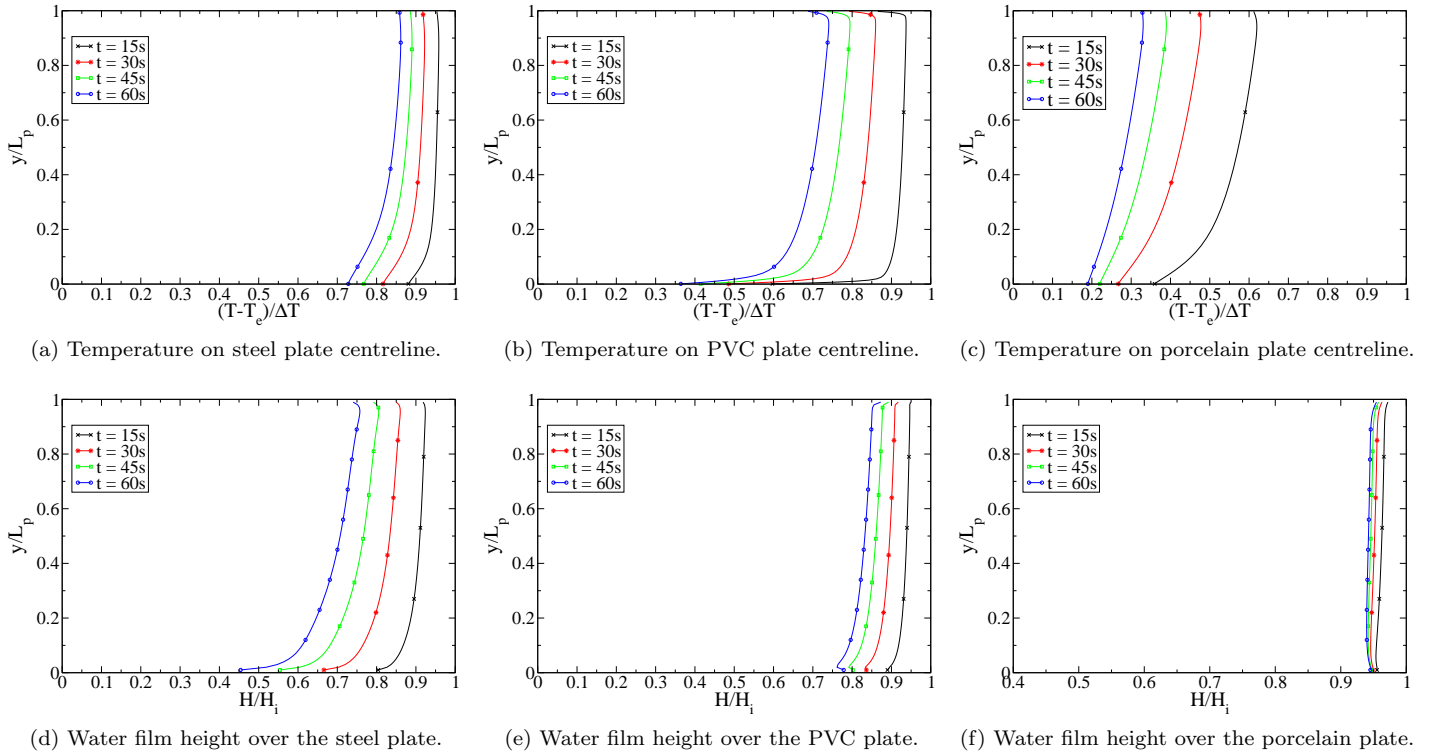


Figure 10: Plate scalar distribution for drying-process simulations, average in spanwise direction. First row: non-dimensional temperature profile on the plate vertical centreline; second row: non-dimensional water film height onto the plate vertical wall.

fect is negligible; thus, the temperature over the centreline and on the plate surface are essentially the same.

Figures 10a,b,c show that the temperature decrement is ruled by the material heat capacity: the lower ρC_p is, the higher the plate cooling is. Table 2 summarises the thermal coefficients and parameters of the three materials under consideration. For all cases, the plate bottom region, $y/L_p \lesssim 0.1$, experiences the higher cooling. This is due to the contact with drier air from the bottom-half cavity, that supports evaporation. In the upper zone, $0.1 \lesssim y/L_p$, temperature distribution is more homogeneous, and the decrease time-rate is in agreement with Figure 6a.

When the plate is made of steel, a smooth thermal transition from the bottom to the upper zone occurs. Indeed, the high conductivity α_s allows for a fast temperature diffusion in vertical direction (cf. the vertical characteristic diffusion times τ_{ver}). In the upper zone, the vertical T gradient is negligible. The PVC plate exhibits a sharp drop of temperature at bottom edge. Since PVC is a strong thermal insulator, the plate internal conduction is not as fast as in steel to supply heat on the bottom zone; indeed, it has a quite high τ_{ver} . The porcelain plate has similar conduction coefficient as steel, then it has a smooth final thermal profile. However, the strong initial cooling process causes a large drop of temperature in the bottom zone, that can be just partially recovered by internal conduction, eventually leading to a vertical temperature gradient in the first

profile, at $t = 15s$.

Figures 10d,e,f show that the evaporation process is directly influenced by temperature. Again, the reduction rate is in agreement with the time evolution of the averaged film thickness, reported in Figure 6c. Steel case has a downward reduction of water film, stronger in the bottom zone. This is due to the intense evaporation supported by the impact of dry air coming from the bottom-half cavity region, as above mentioned. PVC case displays an almost homogeneous H reduction, but there is a minimum peak in the bottom end point. It is generated by the strong temperature drop already discussed. Porcelain case exhibits a negligible decrease of water film. Evaporation occurs mainly during the first seconds, and it is almost homogeneous along the plate surface.

Figure 11 reports the non-dimensional temperature and film thickness distributions on the cavity ceiling, for the final time $t = 160t_0$. The scalars are averaged in spanwise direction. The transitory configurations are not reported, since they show a simple linear increase of all quantities. Temperature profile over the ceiling centreline is the same as at the interface, because of the high characteristic conduction time of steel.

By virtue of symmetry, we focus our attention in the left ceiling side, $y/2L < 0.5$. Three different regions can be identified:

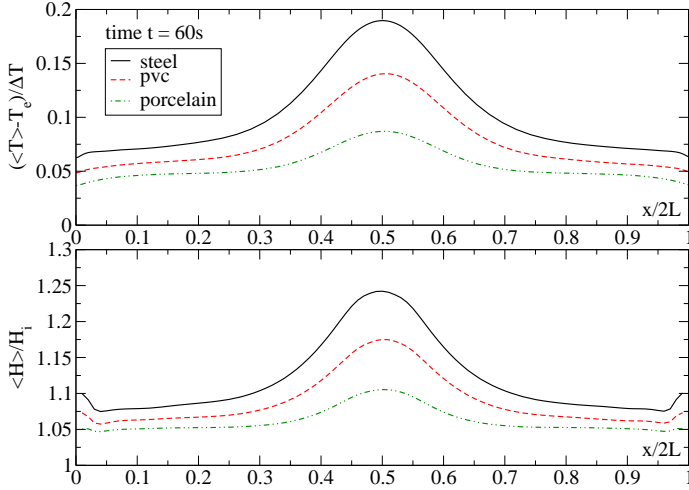


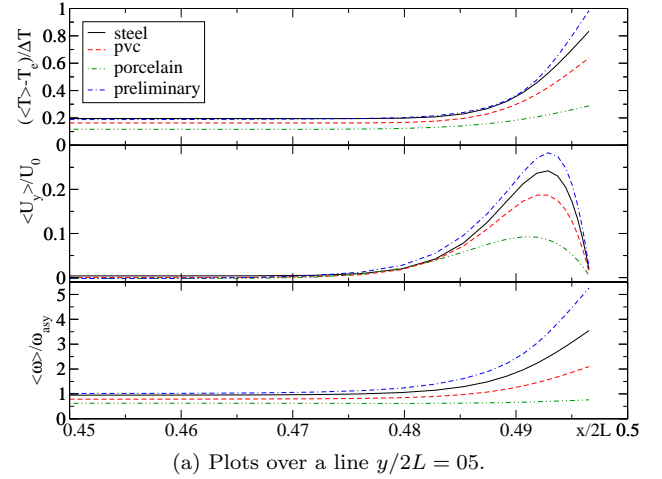
Figure 11: Scalar distribution on enclosure ceiling for drying-process simulations. Top figure, non-dimensional temperature over the ceiling centreline; bottom figure, non-dimensional water film thickness over the ceiling.

- impinging area $0.5 \geq y/2L \gtrsim 0.3$. The ascending plume of hot and humid air impinges the ceiling in this area. At the point $y/2L = 0.5$, film thickness and temperature peak; then T is partially diffused by steel conduction, while H is not subject to this phenomenon (for this reason film thickness decreases more rapidly than temperature when $y/2L \rightarrow 0.3$);
- intermediate area $0.3 \gtrsim y/2L \gtrsim 0.05$. The underlying flow is almost horizontal and both temperature and film thickness experience a moderate decrease;
- corner area $0.05 \gtrsim y/2L \geq 0$. Roughly, it corresponds to the flow corner vortex zone. Temperature slightly decreases, due to diffusion effects. On the other hand, the film thickness sharply increases due to local lower temperature.

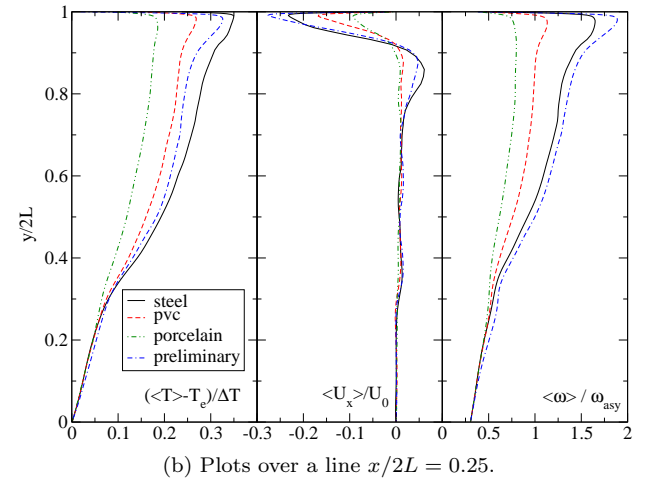
The behaviour of the ceiling is qualitatively unaltered when the plate material is varied. As expected, the values of the scalars are higher for materials that maintain hotter and more humid air.

The distributions on the enclosure vertical wall and floor, are briefly discussed here on. The left and right vertical walls display a linear distribution of both T and H , in accordance with Figure 5. Temperature is maximum at the top and decreases linearly going downward. Vertical walls are warmer for steel case than for porcelain one (as for the ceiling), while PVC case shows an intermediate behaviour. The same holds for film thickness.

The floor maintains essentially unaltered the initial temperature. An almost negligible temperature increase is detected near the corner, as an effects of thermal conduction from the vertical walls.



(a) Plots over a line $y/2L = 0.5$.



(b) Plots over a line $x/2L = 0.25$.

Figure 12: Averaged of non-dimensional temperature, velocity components, vapour concentration for final time configuration.

5.2.5. Local profiles

The general flow features are now investigated on suitable locations. The preliminary and drying-process simulations are reported for the final time $t = 160t_0$, and the quantities are averaged both in spanwise direction and for a short time interval, as in section 5.2.3.

Figure 12a depicts the non-dimensional temperature, vertical velocity and vapour concentration over a horizontal line at level $y/2L = 0.5$, near the plate surface. Other levels are not reported since they do not show significant differences.

In all cases, the air dynamics is confined in a tiny boundary layer. This is not affected by the main fluid motion, because the diagonal-flow and the above ascending region directly merge together, without involving the near-plate flow. Conversely, the boundary layer is controlled by the plate temperature. All quantities are in accordance with the plate temperature evolution. It is interesting that the vapour concentration, unlike temperature and velocity, decreases uniformly for the different materials. This effect

can be explained considering the boundary condition (10) for ω : the function $\omega_T(T)$ is not linear with temperature, but it decreases more for higher temperatures than for lower ones. Thus, the preliminary case and steel case exhibit approximately the same drop of vapour concentration that the PVC and porcelain cases; even if the difference of temperature between the former is smaller than between the latter.

Figure 12b reports the non-dimensional temperature, horizontal velocity and vapour concentration over a vertical line at the mid distance from the plate and the left vertical wall ($x/2L = 0.25$). Temperature and vapour concentration are highly correlated.

In cavity bottom zone ($y/2L \lesssim 0.3$) all the profiles are practically unaffected by variation of the plate material. This is the region where fluid is not influenced by the upper region, thank to the thermal-vapour stratification, and it is almost at rest. In central zone ($0.3 \lesssim y/2L \lesssim 0.7$) conduction is the main heat transfer mode, since the horizontal and vertical (not reported) velocity components are almost zero. In upper zone ($0.7 \lesssim y/2L$) convection dominates and profiles exhibit different behaviour, depending on the plate material.

Steel case and the preliminary one are particularly interesting. Figure 12b shows that the horizontal velocities are similar in the two cases: near the ceiling, in correspondence of the horizontal-flow ($y/2L \gtrsim 0.9$), air flows towards the enclosure vertical wall; just above, in correspondence of the diagonal-flow ($0.8 \lesssim y/2L \lesssim 0.9$) it flows in the opposite direction. These two flows affect the vapour profile: the former transports humid air from the plate, leading to a slight increase of vapour concentration; the latter transports dryer air from the enclosure and decreases ω . The vapour concentration in the horizontal flow region is higher for preliminary case, because isothermal plate maintains higher level of evaporation. Temperature has an opposite behaviour. The preliminary simulation is affected by the stronger cooling effect of the enclosure walls. As a result, the temperature near the ceiling is lower than in the steel case. Also the diagonal-flow (that comes from the vertical wall) decreases air temperature. In the steel case the enclosure is warmed up by the CHT. Thus, air is maintained warmer near the ceiling and in the diagonal-flow region.

Figure 13 displays the non-dimensional temperature, vertical velocity and vapour concentration over three horizontal lines at levels $y/2L = 0.8, 0.5, 0.2$, near the vertical wall enclosure.

Figure 13a shows temperature profiles. At the top ($y/2L = 0.8$) and mid ($y/2L = 0.5$) levels, the distributions are in agreement with Figure 12b: for steel case, temperature is maintained higher than in preliminary case, due to the higher temperature of the enclosure walls. The behaviour at the bottom ($y/2L = 0.2$) level is somehow interesting. Non-dimensional temperature values are one order of magnitude lower than in the other plots. Close to the wall, the profiles are affected by the enclosure temperature: steel maintains higher values since it is able to warm

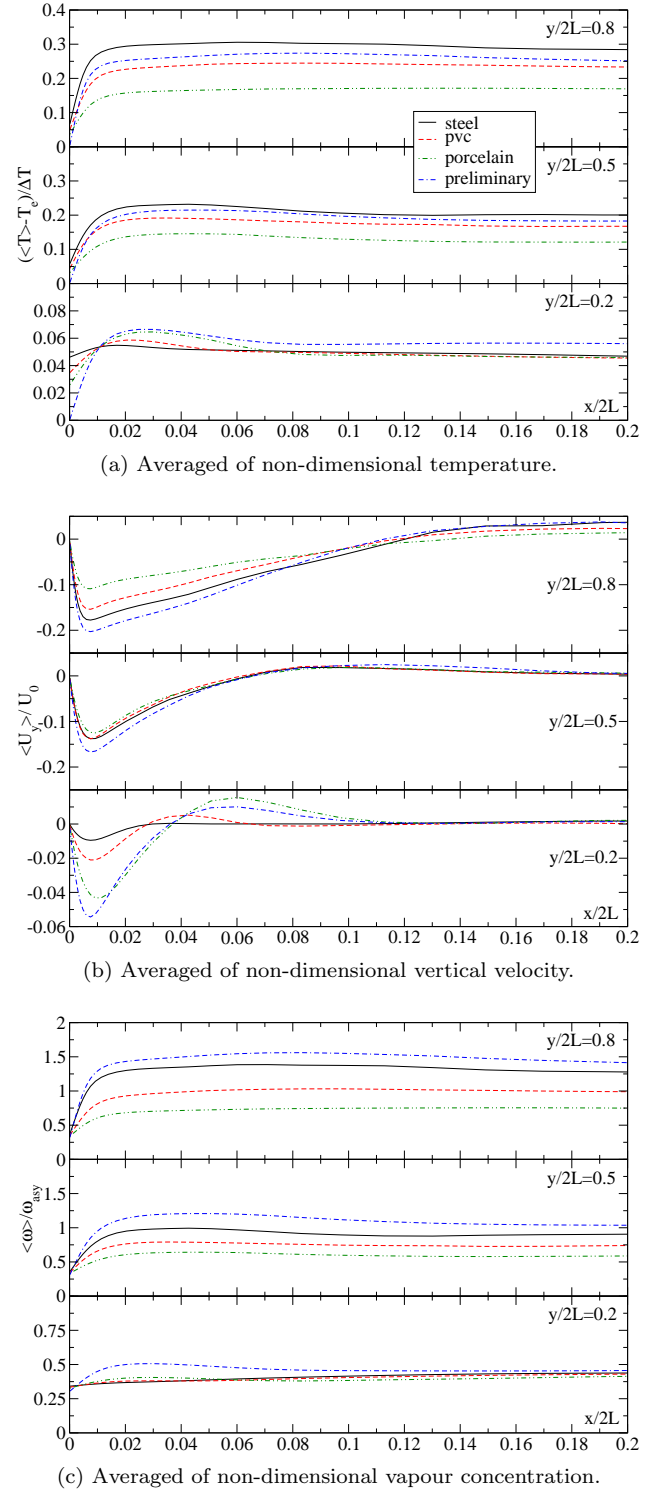


Figure 13: Spanwise and partial time average of non-dimensional temperature, vertical velocity, vapour concentration for final time configuration. Plots over lines near the vertical enclosure wall, at three height $y/2L = 0.8, 0.5, 0.2$, respectively from the top to the bottom in each figure.

up the wall, while in the preliminary case temperature decreases to the value of the isothermal cold wall. Farther from the wall influence, about $x/2L \gtrsim 0.01$, the order is reversed: in porcelain and preliminary simulations, temperature slightly increases with respect to steel and PVC cases. This effects can be explained taking into account the velocity profiles in Figure 13b: since the hot air coming from the upper-half on the cavity is diffused by convection, the higher vertical velocity of porcelain and preliminary cases allow for a higher temperature.

Figure 13b reports the vertical velocity component. At the top level, the flow is governed by the buoyancy force generated by the thermal gradient between enclosure and fluid: cases with lower wall temperature exhibit higher velocity. At the mid level, the differences among drying-process simulations disappear. Indeed, in the bottom-half of the cavity the strong thermo-solutal stratification takes place: the buoyancy force generated by the wall is balanced by the opposite buoyancy force due to the underlying cold and dry air. In the bottom level the balance between these two forces breaks. Steel and PVC cases, that have stronger stratification (cf. Figures 8, 9), experience a velocity decrease; while porcelain case, that is not stratified, maintains higher velocity. The preliminary case is an exception, as it is highly stratified but has the highest velocity. This is due to the larger buoyancy force generated by the thermal and humidity gradient at the vertical wall, that overcomes the stratification counter force. Farther from the wall ($0.04 \lesssim y/2L$) porcelain and preliminary cases have positive velocity values. This is the area where the diagonal-flow starts. PVC case has lower values. Steel case does not show any positive velocity, meaning that the diagonal-flow starts from higher level.

Figure 13c depicts the vapour concentration distribution. At the top and mid levels, condensation decreases ω near the wall. Further from the wall, the profiles are coherent with temperature: when air is more warm, it is also more humid. At the bottom level, there are no differences among the cases. Vapour does not condense, thus there is no near wall decrease. In Figure 13a we have notice that porcelain and preliminary cases have high temperature profile at bottom level (with respect to steel and PVC cases); hence also a higher vapour value is expected. Preliminary simulation exhibits higher ω , but porcelain case doesn't. The reason is that, in porcelain case, evaporation stops and the humidity in the cavity is low. Hence, convection cannot bring significant amount of vapour towards the bottom region.

6. Conclusions

Evaporation and condensation in a turbulent buoyancy driven flow are studied *via* large-eddy simulations. The dynamic Lagrangian sub-grid scales model is chosen to compute the SGS viscosity, along with the SGS thermal and vapour diffusivity. The presence of water phase is modelled by a thin water film. The solid-fluid thermal

coupling is taken into account through the conjugate heat transfer procedure described in Sosnowski [31] (conduction), and by the evaporation source/condensation sink boundary term described in Petronio [25] (water change of phase). The numerical solver is developed within the OpenFOAM software framework.

The case of a vertical hot plate inside a cold enclosure, filled with humid air, is studied. Both the plate and the enclosure are initially wet by a thin water film, and the enclosure is thermally isolated from outside. Evaporation from the plate and the subsequent cooling process is investigated. The numerical solver has been validated in Cintolesi *et al.* [7] for what concern the fluid dynamics and the CHT procedure; and in Petronio [25] for evaporation/condensation model.

First, a preliminary case is simulated: the water film thickness is not allowed to change and the CHT is not considered. Anyway, water can evaporate and condensate. The result is a statistical steady state configuration, where the buoyancy flow is generated near the plate and the top vertical enclosure walls. This preliminary configuration is characterised by a Rayleigh number of $Ra = 5 \times 10^8$.

The absence of surface thermal interaction leads to an analogous distribution of temperature and vapour, as expected after an analysis of the mathematical model. A realistic reproduction of thermal and humidity distribution cannot be achieved neglecting the solid-fluid surface heat transfer. A strong thermal and humid stratification arises: the cavity is sharply divided into a warm and humid top region, and a relative cold and dry bottom part. The general flow is described and three main regions of motion are identified. The stable stratification inhibits the formation of recirculation regions developing along the entire cavity height. Instead, smaller recirculation vortexes appear in the top half-cavity.

An additional simulation with dry air is performed, using the same setting as the preliminary simulation. The comparison between the dry and humid air cases shows that the velocity magnitude is considerably increased by the presence of water vapour. The heat transfer rate is analysed in the two cases, pointing out that the latent heat flux rules the heat exchange process, as expected.

Successively, the CHT and water film model are switched on and three simulations are performed, changing the plate material, in order to study the different evolution of the system. The materials are chosen to have different thermal properties. The complete evaporation of water film can require a long physical time, thus it is not entirely simulated. We reproduce the first 60s of the physical time, when the systems are still in transitional phase. This period is crucial to investigate the influence of different plate materials on the overall fluid dynamics. Heat transfer by evaporation and condensation is found to overcome the other heat transfer modes during the cooling of the plate. The thermal inertia of the medium ρC_p is the parameter that controls the cooling process: high values of thermal inertial cause a slight decrease of temperature,

whereas low values lead to fast cooling. As soon as the plate loses heat, the overall flow velocity is reduced and the thermal and vapour stratification become weaker.

The average plate temperature evolution in time is reported: high- ρC_p materials show a linear temperature reduction, while low- ρC_p materials display an initial sharp and a subsequently moderate heat loss. The plate film thickness and air vapour concentration evolve according to temperature behaviour. The water film exhibits a negligible reduction for low- ρC_p , whereas the reduction is between 20 – 30% for high- ρC_p . At the enclosure surfaces, the condensation takes place mainly onto the ceiling, in a narrow region just above the plate, where the hot and humid air impinges the wall.

An analysis of the dew-point temperature suggests that, for the cases herein examined, even for materials that are rapidly cooled down, the vapour recondensation onto the plate surface cannot occur.

Acknowledgements

This research has been carried out using computational facilities procured through the European Regional Development Fund, Project ERDF-080 “A Supercomputing Laboratory for the University of Malta”.

References

- [1] AA. VV., *Programmers Guide - version 2.1.0*, OpenFOAM Foundation, 15th December 2011.
- [2] AA. VV., *User Guide - version 2.1.0*, OpenFOAM Foundation, 15th December 2011.
- [3] *ASHRAE Handbook Fundamentals - SI edition*, Ed. Ashrae, 2005.
- [4] V. ARMENIO AND S. SARKAR, *An investigation of stably stratified turbulent channel flow using large-eddy simulation*, *J. Fluid Mechanics*, 459 (2002), p. 1.
- [5] A. W. T. BARENBRUG, *Psychrometry and Psychrometric Charts*, Cape and Transvaal Printers Ltd., 3rd ed., 1974.
- [6] A. BUKHVOSTOVA, E. RUSSO, J. KUERTENA, AND B. GEURTS, *Comparison of dns of compressible and incompressible turbulent droplet-laden heated channel flow with phase transition*, *Int. J. of Heat and Fluid Flow*, 50 (2014), p. 445.
- [7] C. CINTOLESI, A. PETRONIO, AND V. ARMENIO, *Large eddy simulation of turbulent buoyant flow in a confined cavity with conjugate heat transfer*, *Physics of fluids*, 27 (2015). doi: 10.1063/1.4930815.
- [8] V. A. F. COSTA, *Transient natural convection in enclosures filled with humid air, including wall evaporation and condensation*, *Int. J. Heat and Mass Transfer*, 55 (2012), p. 5479.
- [9] M. DAS AND K. REDDY, *Conjugate natural convection heat transfer in an inclined square cavity containing a conducting block*, *Int. J. of Heat and Mass Transfer*, 49 (2006), p. 4987.
- [10] P. G. DE GENNES, *Wetting: statics and dynamics*, *Reviews of Modern Physics*, 57 (1985), p. 827.
- [11] A. DORFMAN AND Z. RENNER, *Conjugate problems in convective heat transfer: Review*, *Mathematical Problems in Engineering*, 2009 (2009).
- [12] F. DUCHAINE, A. CORPRON, L. PONS, V. MOUREAU, F. NICLOUD, AND T. POINSOT, *Development and assessment of a coupled strategy for conjugate heat transfer with large eddy simulation: application to a cooled turbine blade*, *Int. J. Heat and Fluid Flow*, 30 (2009), p. 1129.
- [13] F. DUCHAINE, S. MENDEZ, F. NICLOUD, A. CORPRON, V. MOUREAU, AND T. POINSOT, *Conjugate heat transfer with large eddy simulation for gas turbine components*, *Comptes Rendus Mecanique*, 337 (2009), p. 550.
- [14] C. HUANG, W. YAN, AND J. JANG, *Laminar mixed convection heat and mass transfer in vertical rectangular ducts with film evaporation and condensation*, *Int. J. of Heat and Mass Transfer*, 48 (2005), p. 1772.
- [15] F. INCROPERA, D. DEWITT, T. BERGMAN, AND A. LAVINE, *Fundamentals of heat and mass transfer*, John Wiley and Sons Inc., 6th ed., 2007.
- [16] C. ISKRA AND C. SIMONSON, *Convective mass transfer coefficient for a hydrodynamically developed airflow in a short rectangular duct*, *Int. J. of Heat and Mass Transfer*, 50 (2007), p. 2376.
- [17] N. LAAROSSI AND G. LAURIAT, *Conjugate thermosolutal convection an condensation of humid air in cavity*, *Int. J. Thermal Sciences*, 47 (2008), p. 1571.
- [18] O. LAGUERRE, S. BEN AMARA, G. ALVAREZ, AND D. FLICK, *Transient heat transfer by free convection in a packed bed of spheres: comparison between two modelling approaches and experimental results*, *Appl. Therm. Eng.*, 28 (2008), p. 14.
- [19] O. LAGUERRE, S. BEN AMARA, AND D. FLICK, *Numerical simulation of simultaneous heat and moisture transfer in a domestic refrigerator*, *Int. J. of Refrigeration*, 33 (2010), p. 1425.
- [20] O. LAGUERRE, S. BEN AMARA, D. REMY, AND D. FLICK, *Experimental and numerical study of heat and moisture transfers by natural convection in a cavity filled with solid obstacles*, *Int. J. of Heat and Mass Transfer*, 52 (2009), p. 5691.
- [21] M. G. LAWRENCE, *The relationship between relative humidity and the dewpoint temperature in moist air: A simple conversion and applications*, *Bulletin American Meteorological Society*, 86 (2005), p. 225.
- [22] J. LIENHARD IV AND J. LIENHARD V, *A heat transfer textbook*, Phlogiston Press - Cambridge, 2.02 ed., 2012.
- [23] C. MENEVEAU, T. LUND, AND W. CABOT, *A lagrangian dynamic subgrid-scale model of turbulence*, *J. Fluid Mechanics*, 316 (1996), p. 353.
- [24] A. ORON, S. DAVIS, AND S. BANKOFF, *Long-scale evolution of thin liquid films*, *Reviews of Modern Physics*, 69 (1997), p. 931.
- [25] A. PETRONIO, *Numerical investigation of condensation and evaporation effects inside a tub*, Ph.D. thesis, School of Environmental and Industrial Fluid Mechanics, University of Trieste, 2010. NBN urn:nbn:it:units-9122.
- [26] U. PIOMELLI, *Large-eddy and direct simulation of turbulent flows*, CFD2001 - 9th Conférence Annuelle de la Société Canadienne de CFD, 2001.
- [27] A. RAIMUNDO, A. GASPARELLO, A. VIRGILIO, M. OLIVEIRA, AND D. QUINTELA, *Wind tunnel measurements and numerical simulations of water evaporation in forced convection airflow*, *Int. J. of Thermal Sciences*, 86 (2014), p. 28.
- [28] E. RUSSO, J. KUERTEN, C. VAN DER GELD, AND B. GEURTS, *Modeling water droplet condensation and evaporation in dns of turbulent channel flow*, *J. of Physics Conference Series*, 318 (2011).
- [29] P. SAGAUT, *Large eddy simulation for incompressible flows. An introduction*, Springer, 2000.
- [30] P. SOSNOWSKI, *Numerical investigation of evaporation and condensation of thin films in conjugated heat transfer systems*, Ph.D. thesis, School of Environmental and Industrial Fluid Mechanics, University of Trieste, 2013. NBN urn:nbn:it:units-10080.
- [31] P. SOSNOWSKI, A. PETRONIO, AND V. ARMENIO, *Numerical model for thin liquid film with evaporation and condensation on solid surfaces in a systems with conjugated heat transfer*, *Int. J. Heat and Mass Transfer*, 66 (2013), p. 382.
- [32] H. SUN, G. LAURIAT, AND X. NICOLAS, *Natural convection and wall condensation or evaporation in humid air-filled cavities subjected to wall temperature variations*, *Int. J. Thermal Sciences*, 50 (2011), p. 663.
- [33] P. TALUKDAR, C. ISKRA, AND C. SIMONSON, *Combined heat and*

mass transfer for laminar flow of moist air in a 3d rectangular duct: Cfd simulation and validation with experimental data, Int. J. of Heat and Mass Transfer, 51 (2008), p. 3091.

- [34] U. THIELE, *Structure formation in thin liquid films*, vol. 490, CISM International Centre for Mechanical Sciences, 2007. Chapter: Thin Films of Soft Matter.
- [35] J. WELTY, C. WICKS, R. WILSON, AND G. RORRER, *Fundamentals of momentum, heat, and mass transfer*, John Wiley and Sons Inc., 5th ed., 2008.